

Shear and Baroclinic Energy Flux on the Summer New England Shelf

J. A. MACKINNON* AND M. C. GREGG

Applied Physics Laboratory and Department of Oceanography, University of Washington, Seattle, Washington

(Manuscript received 24 February 2002, in final form 3 December 2002)

ABSTRACT

Observations are presented of internal wave properties and energy fluxes through a site near the 70-m isobath on the New England shelf in late summer. Data collected from a shipboard ADCP and microstructure profiler over a three-week period and projected onto dynamic vertical modes reveals large variations in the magnitude and vertical structure of internal waves. Baroclinic energy and shear were primarily associated with low-mode near-inertial and semidiurnal waves and, at times, high-frequency solibores. The energies in each mode varied by factors from 2 to 10 over several days and were not significantly correlated with one another. The associated shear variance was concentrated in the thermocline. However, the strength and vertical range of shear varied significantly throughout the research period and depended sensitively on both the magnitude and evolving vertical mode content of the wave field. Shear during the quasi-two-layer solibores was strong enough to temporarily lower the 4-m Richardson number below the threshold for shear instability. Energy flux through the site came primarily from the mode-1 internal tide, in both linear and nonlinear (solibore) forms. The average energy flux from the first five baroclinic modes was 130 W m^{-1} . A comparison of energy fluxes from each mode and locally measured average dissipation rates suggests that near-inertial and high-mode waves were generated near the experimental site.

1. Introduction

Internal waves on continental shelves may be important sources of energy dissipation for the global oceanic energy budget and local mixing. Onshore propagating internal tides and wind-generated near-inertial waves are commonly found on continental shelves around the world, usually with large temporal variability (e.g., Holloway et al. 2001). Strong, nonlinear solitons are often associated with the internal tide (Sandstrom and Oakey 1995; Colosi et al. 2001). The term “solibore” (Heney and Hoering 1997) may be a more accurate term, reflecting both the soliton and borelike characteristics of these waves, which can also be thought of as a steepening of the leading edge of the internal tide. Turbulent energy dissipation may be diagnosed or modeled as a function of the local shear field (Gregg 1989; Polzin et al. 1995), which is in general a complicated function of the time varying energy and vertical structure of the waves present. Turbulence can in turn drain energy from internal waves. The rate of energy flux through a given location controls the amount of energy

available for mixing elsewhere (upshelf for an onshore propagating wave).

The Coastal Mixing and Optics (CMO) experiment provided a unique opportunity to combine measurements of the internal wave field and turbulence microstructure. Here observations are presented of the local energy and shear fields at a fixed location on the New England shelf during late summer and the magnitude and flux of energy through our site. In a companion paper, MacKinnon and Gregg 2003a (hereinafter referred to as MGa), we compare these wave field measurements with estimates of turbulent dissipation and mixing.

Section 2 describes our instruments and measurement techniques. Section 3 presents measurements and analysis of internal wave energy and shear, with a focus on low-frequency waves and solibores. In section 4, we calculate the flux of wave energy through the observational site. Using two complimentary methods, we compute the direction and magnitude of energy flux for distinct vertical modes, wave groups and solibores. Conclusions are presented in section 5.

2. Experimental methods

a. Experiment

From 19 August to 1 September 1996 we obtained water property and velocity data on the New England shelf on board the R/V *Seward Johnson* near the 70-m isobath south of Nantucket in a region known as the

* Current affiliation: IOD/SIO, La Jolla, California.

Corresponding author address: Dr. J. A. MacKinnon, IOD/SIO, 9500 Gilman Drive, Mail Code 0209, La Jolla, CA 92093-0209.
E-mail: jen@coast.ucsd.edu

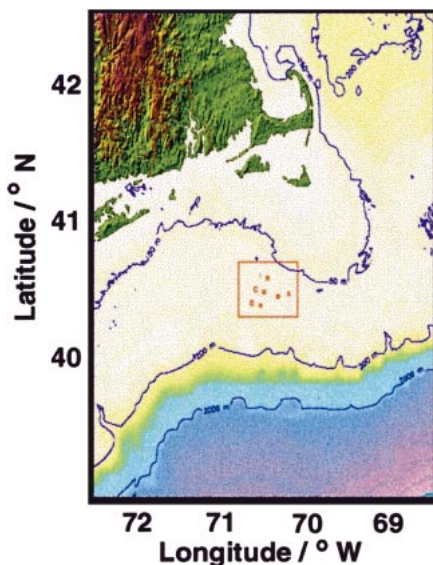


FIG. 1. Location of the CMO experiment. Profiling took place near the central site (labeled “C”), in a region 1.5 km wide (not shown).

“mud patch” for its fine sediments (Fig. 1). The vessel steamed slowly east and west (to prevent the profiler from moving under the ship) in a box 1.5 km long (along shelf) and 1 km wide (across shelf) centered near 40°30'N, 70°30'W. On 1 September we were forced into port by Hurricane Edouard. We returned on 4 September for several more days of work. Posthurricane data are presented in MGa. Our date convention is that noon of 1 January is yearday 0.5.

b. Profiler measurements

Temperature and salinity measurements were made with SeaBird sensors mounted on the Modular Microstructure Profiler (MMP), a loosely tethered, free-falling instrument ballasted to fall at 0.5 m s⁻¹. Generally profiling in 12-h shifts at night, we completed a full water column profile approximately every four minutes during peak operating efficiency, resulting in 1469 profiles before the hurricane. By monitoring data from a small acoustic altimeter attached to the MMP, we were able to safely profile to within a few meters of the bottom. Though MMP quantities are measured as a function of pressure, all quantities are plotted versus depth for comparison with acoustic Doppler current profiler data, which produces an average error of less than 1%.

c. Velocity

Two shipboard broadband ADCPs operated continuously throughout the cruise and provided velocity data in 4-m vertical bins between 12 and 56 m (150 kHz), and 1-m bins between 8 and 32 m (600 kHz), though the higher noise of the 600-kHz instrument precluded reliable resolution of scales below 2–3 m. The ADCP

sampling applies an effective 8-m Bartlett filter to the 150-kHz data and an effective 2-m filter to the 600-kHz data; hence only every other depth bin is truly independent. An 8-m Bartlett filter was applied to the 600-kHz data to mimic this effect and give the same resolution for all data. In our analysis we use composite velocity data, which combined both ADCPs at 4-m intervals to span the broadest range of the water column (velocities were averaged in the depth range of instrument overlap). Baroclinic velocity was computed by removing the depth-mean of each velocity component. Shear was calculated by first-differencing composite velocity over 4-m intervals. There is a loss in shear variance due to both the first-differencing process and the Bartlett filter response. Though specific phase information of the lost shear cannot be regained, we estimated that average 4-m shear variance would be 1.5 times the variance we measured based on spectra of observed shear and knowledge of the filter transfer functions. This is smaller than the factor of 2.11 used by Gregg (1989), most likely because of the lower vertical mode nature of this internal-wave field. Additional variance loss due to beam separation was also possible (Alford and Pinkel 2000). None of the variance loss estimates were used to correct the data.

3. Observations of internal waves and shear

In this section, we present observations and statistics of internal waves and associated shear. The focus is on internal wave features that are related to specific observations of turbulence in MGa or statistics that can be directly compared with internal-wave-based models of turbulence. In pursuit of the first goal, we discuss two primary sources of the shear variance that is linked to turbulence in MGa—low-mode, low-frequency waves and high-frequency solibores. We start with a brief description of the background through which internal waves propagate.

a. Water properties and barotropic flow

Water on the shelf was strongly stratified, with a thermocline typically between 15 and 20 m (Fig. 2). Changes in stratification reflected divergences in vertical wave velocities and horizontal advection of local gradients, the later identifiable through *T/S* variability (MGa; Gardner et al. 2001). Density changes can be used to calculate a perturbation pressure that is later used to estimate energy fluxes. For hydrostatic waves, perturbation reduced pressure (dimensional pressure divided by an average density, ρ_0) is given by (Kunze et al. 2002)

$$p'(z) = \frac{g}{\rho_0} \left[\int_z^0 \rho'(z') dz' - \frac{1}{H} \int_{-H}^0 \int_z^0 \rho'(z') dz' dz \right] \text{ J kg}^{-1}, \quad (1)$$

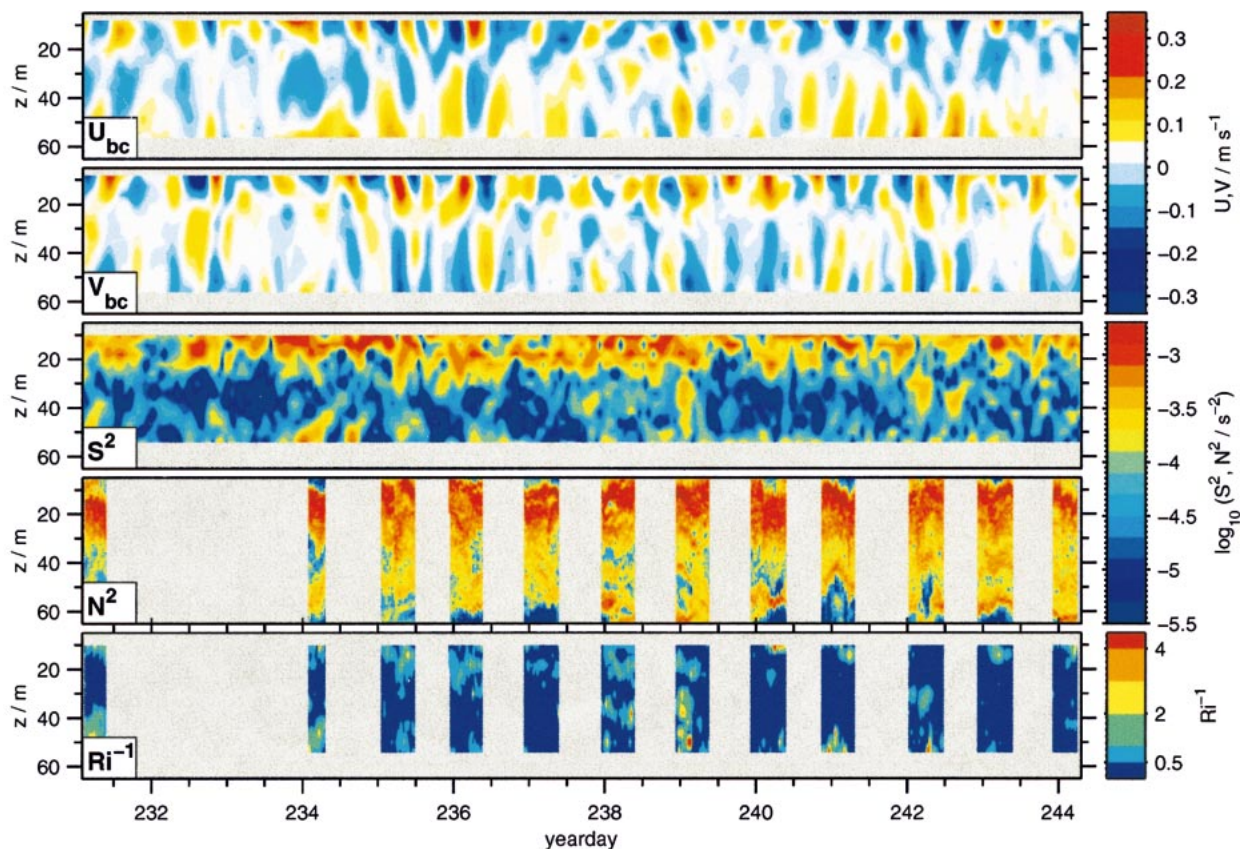


FIG. 2. From top to bottom: low-passed (below 0.17 cph) eastward and northward baroclinic velocity, low-passed shear variance, stratification during MMP profiling periods, and inverse Richardson number from 4-m shear and stratification.

where ρ' is the density perturbation from a slowly evolving mean density profile. For calculation of the low-passed density profile, our data were supplemented with a time series of CTD data generously provided by W. Gardner, Texas A&M University. The second term within the brackets ensures that perturbation pressure is baroclinic (has a zero depth average). Pressure perturbations were dominated by a low-mode structure (Fig. 3).

The high-frequency thermocline depressions associated with solibores are visible as sharp perturbation pressure events during, for example, yeardays 235, 241, and 242.

Barotropic (depth averaged) flow primarily consisted of a nearly circular mixed tide ($0.11 \pm 0.06 \text{ m s}^{-1}$) superimposed on a comparably strong along-shelf flow ($0.11 \pm 0.04 \text{ m s}^{-1}$), where the range given is the standard deviation. The combination at times produced large

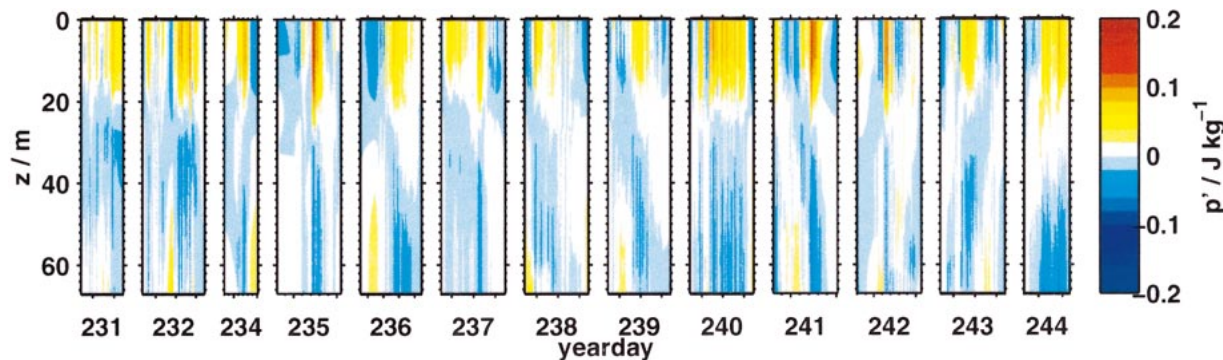


FIG. 3. Perturbation pressure calculated from MMP density measurements. The boxes represent MMP profiling periods with a date representative of most data during that period. The relative widths of the boxes are proportional to the relative durations of profiling, but the spaces between boxes are not to scale. See Figs. 2 and 4 for the relative times of each profiling period.

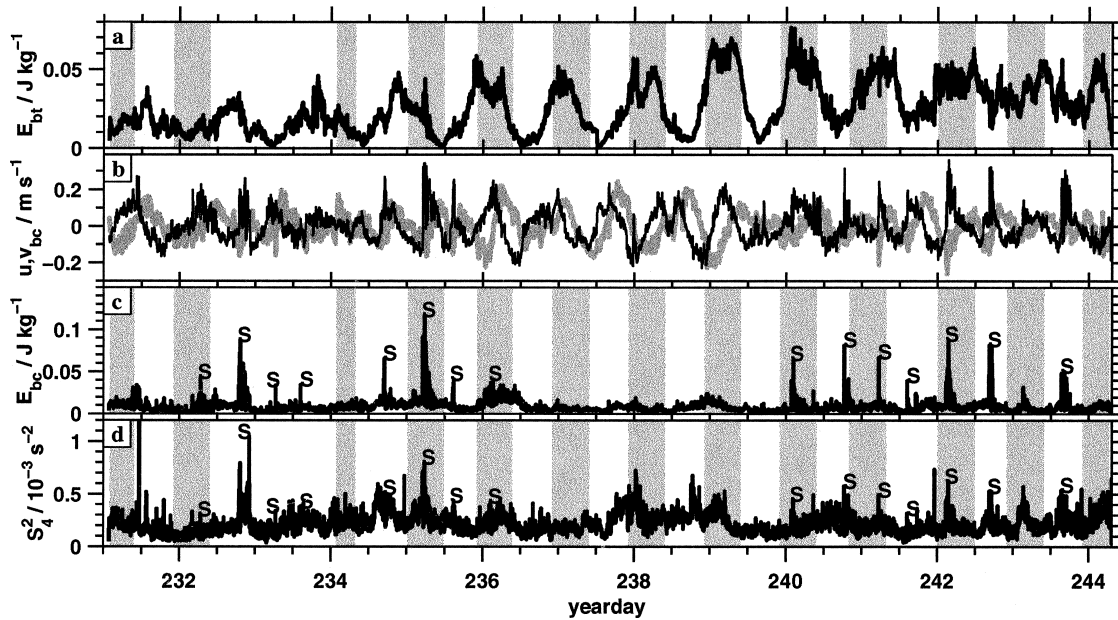


FIG. 4. (a) Depth-averaged barotropic energy, with MMP profiling periods indicated by gray shading; (b) eastward (gray, thick) and northward (black, thin) baroclinic velocity at depth 16 m, profiling periods hidden for clarity; (c) depth-averaged baroclinic energy; and (d) depth-averaged shear variance. Solibore times (as defined in section 3b) are indicated with an S.

variations in barotropic energy (Fig. 4a). Observations of tidal and subtidal flow were consistent with previous studies in this area (Voorhis et al. 1976; Chapman and Beardsley 1989; Sundermeyer and Ledwell 2001).

b. Internal wave observations

The baroclinic wavefield consisted of evolving low-frequency, low-mode waves, punctuated by episodic groups of high-frequency solibores. Both phenomena can be observed in time series of baroclinic velocity, depth-averaged baroclinic energy, and shear variance (Fig. 4). Baroclinic energy and shear variance are visually dominated by a series of energetic but short-lived spikes (Figs. 4c, d). Most of these events appear as pulses of northward velocity at 16 m (Fig. 4b). There is a large body of theoretical and observational work describing such high-frequency, nonlinear motions as solitons or solibores; they are considered further in section 3d.

There is also a low-frequency, clockwise wave apparent in baroclinic velocity, especially near yeardays 231–232, 236–239, and 242 (Fig. 4b). The flow is nearly circularly polarized (equal northward and eastward magnitude); hence there is not a strong signal at the wave period in baroclinic energy or shear variance (Figs. 4c, d). Instead, the low-frequency variability in energy and shear variance represents the timescales over which wave energy waxes and wanes. In the remainder of this section attention is restricted to low-passed (below 0.17 cph) motions, which overall make up 84% of baroclinic kinetic energy and 72% of shear variance.

Low-frequency waves had large-scale but variable vertical structures. Figure 2 shows depth–time maps of each component of low-passed baroclinic velocity and the associated shear variance. The vertical structure of velocity suggests low-mode internal waves. On yeardays 231–233 and 240–243, there appeared to be a first-mode, clockwise-polarized, standing wave, with flow above the thermocline ($z \leq 20$ m) in the opposite direction of subthermocline flow. At other times, yeardays 237–238, higher modes were clearly present. Midcolumn shear variance was on average concentrated near the thermocline (depth 10–25 m), consistent with low-mode internal wave structure (Fig. 2). Evolving vertical wave structure at times elevated shear variance below the thermocline (e.g., yearday 238–239).

c. Internal wave statistics

The distribution of energy between vertical modes significantly fluctuated, which has important implications for the magnitude and location of shear variance, as well as for internal-wave-interaction-based models of turbulence production. A linear wave field can be represented as a superposition of internal waves of distinct frequency (ω) and vertical mode number (j), which together determine the magnitude of horizontal wavenumber (e.g., Munk 1981; Levine 2002). The vertical structure of each mode is governed by (Gill 1982; Thorpe 1998; Levine 2002)

$$\Psi_j''(z) = -\frac{N^2(z)}{c_j^2} \Psi_j(z) \tag{2}$$

$$\Psi_j(-H) = \Psi_j(0) = 0, \tag{3}$$

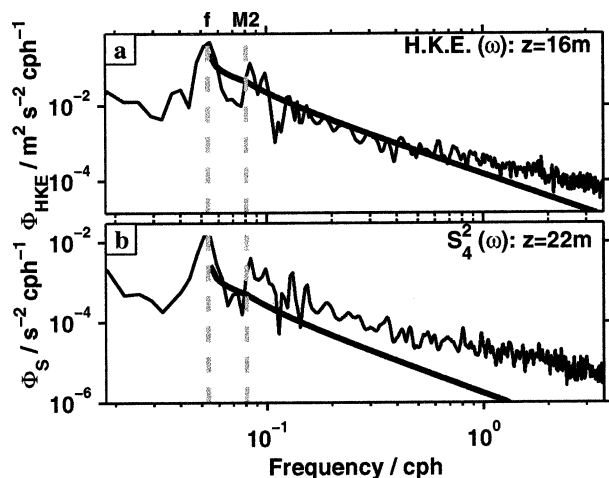


FIG. 5. (a) Rotary spectra (clockwise plus counterclockwise) of baroclinic energy at $z = 16$ m, along with the “moored spectrum” from Levine (2002) using $E_{\text{ref}} = 0.5 \text{ m J kg}^{-1}$. (b) Same but for shear spectra at 22 m. The moored spectrum for shear is calculated from the energy spectrum based on the vertical mode distribution presented in Levine. Inertial and semidiurnal frequencies are indicated for reference. In both plots observed spectra have been smoothed above twice the M_2 frequency for ease of comparison with spectral models.

where c_j is the separation constant (eigenvalue), and waves are assumed to be hydrostatic. Vertical velocity and vertical displacement associated with each mode are proportional to Ψ_j , while the horizontal velocity is proportional to $d\Psi_j/dz$.

Many statistical internal wave models assume that the frequency and vertical mode distributions of wave energy are separable functions. For example, in the enduringly popular Garrett–Munk model (hereinafter GM), as presented in Levine (2002), spectral energy distribution is given as

$$E(\omega, j) = E_{\text{ref}} \hat{B}(\omega) H_j,$$

where E_{ref} is the (assumed slowly evolving) vertically

averaged energy per unit mass (see the appendix for details).

We begin by considering the average frequency content of observed waves. Baroclinic energy and shear display a GM-like spectral slope for a midrange of frequencies, but diverge at both the high and low ends of the spectrum (Fig. 5). There are distinct and significant peaks near inertial and semidiurnal (M_2) frequencies. At the other end, there is an elevated shoulder of energy and shear above 0.5 cph that Levine attributes to high-frequency solitons (section 3d).

The main focus here is on the distribution of energy amongst vertical modes, H_j . There are two motivations for this focus, both ultimately related to internal-wave-generated turbulent mixing. First, higher modes contribute a relatively larger amount of shear. Hence, for a given level of wave energy, the distribution of relative modal energy controls the magnitude and location of shear variance and Richardson number (A12), which in turn determine the likelihood of shear instabilities to occur (Miles 1961; Thorpe 1978). Second, models of mode distribution are explicitly used by recent parameterizations of the turbulent dissipation rate (e.g., MGA; Gregg 1989; Polzin et al. 1995). Such models combine observations of low-mode waves with an assumed steady spectral shape to extrapolate the rate of spectral energy transfer to smaller scales (and hence to mixing) through wave–wave interactions.

In practice, the vertical mode shapes presented here are calculated from numerical solution of (2) using the average stratification profile (Fig. 6). Velocity data were fit to the barotropic and first five baroclinic modes using a least squares minimization. For comparison, we also calculate empirical orthogonal functions (EOFs), those coherent structures that maximize variance between measured velocity at different depths (Fig. 6, gray). The strong similarity between theoretical modes and EOFs is encouraging.

A mode-fit velocity profile was created at each time

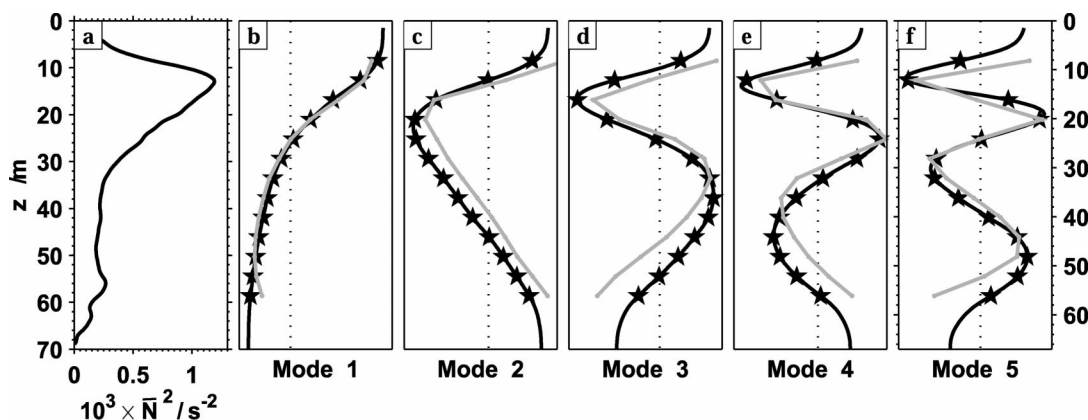


FIG. 6. (a) Cruise-averaged stratification. (b)–(f) Shapes of first five baroclinic modes based on a numerical solution of (2) (black), with ADCP sampling locations indicated by stars. The corresponding EOF shapes are shown in gray; EOFs have been normalized to have the same vertically averaged variance as the corresponding dynamic modes.

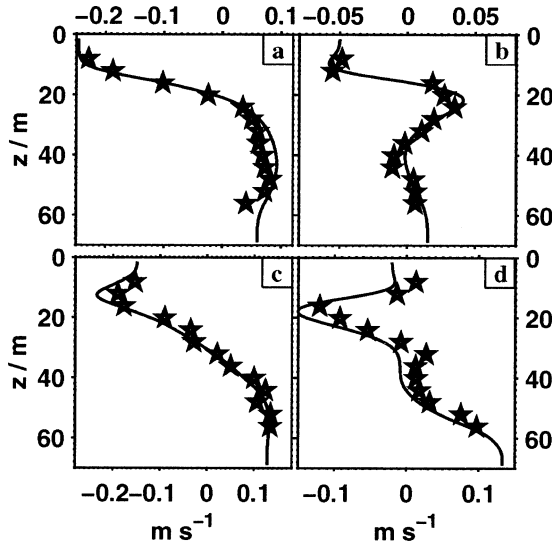


FIG. 7. Measured velocity (stars) and sum of the first five baroclinic mode fits (lines) for (top) eastward and (bottom) northward velocity profiles for two representative times: (left) yearday 235.95 and (right) yearday 238.96.

by combining the projected amplitude and vertical structure of the first five baroclinic modes. Examples of mode-fit eastward and northward velocity during two sample time periods are shown in Fig. 7. The modal fit captures the dominant low-mode signal well, though it does not reproduce the small-scale fluctuations that are a relatively more important part of shear variance. Overall, the mode fit captures 90% of the baroclinic energy and 72% of the shear variance.

On average, low-frequency wave energy was weighted more strongly toward low modes than predicted by the GM H_j distribution, even using $j_* = 1$ as suggested by Levine (2002) (Fig. 8; appendix). The flatter shape of the average shear modal distribution (Fig. 8b) reflects the opposing tendencies of the two components of shear: energy is concentrated in low modes while higher modes contribute more shear (A12).

More important than the particular shape of average mode distribution, the relative strengths of each mode changed significantly and independently during the experimental period. Figure 9a represents the changing relative modal amplitudes by a time series of stacked histograms of low-frequency energy in each mode. Both the total energy, $E(t)$, and the relative contribution of each mode, $H_j = H_j(t)$, changed significantly throughout the cruise (A8). The formal correlation between the amplitudes of different modes was quite low, especially between the lowest and highest measured modes (Table 1). Note that spectral models like GM assume there is no correlation between the phases of individual waves, but they do assume a prescribed relationship between the evolving average energy (amplitude) of low and high modes.

The observation of nonsteady mode distribution is one of the major conclusions of this paper. A thorough analysis of the reasons for spectral variability is beyond the scope of this work, but we can offer two tentative hypotheses. First, variations in the background stratification and mean shear may funnel internal-wave forcing energy into different modes. For example, Mackinnon and Gregg (2003b, manuscript submitted to *J. Phys. Oceanogr.*) argue that changes in stratification and a significant nonlinear bottom drag may alter the modal content of wind-generated near-inertial waves. Additionally, internal tide generation at the shelf edge may be sensitive to the meanders of a strong shelfbreak jet. Second, low-frequency waves have on average a different modal energy distribution than high-frequency waves. In particular, high-mode waves do not have strong peaks at low frequencies (Fig. 10). Changes in the total energy of low-frequency waves hence produce changes in vertical mode content.

Changes in relative modal amplitude decouple the energy and shear content of the wavefield. For example, during yeardays 237–239, there was a relatively large amount of shear from higher modes, while the total energy level was low (Fig. 9b). Changing modal am-

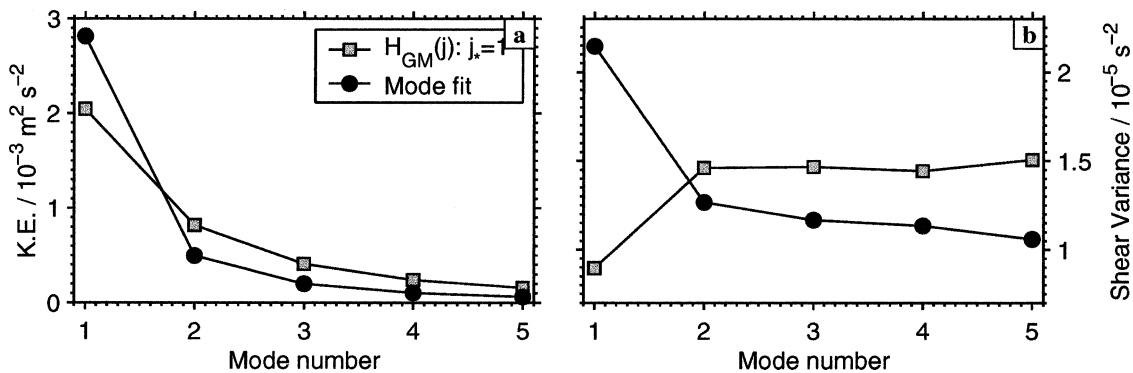


FIG. 8. (a) Horizontal kinetic energy in each mode from modal fits (circles) and the Garrett–Munk modal distribution, H_{GM} , using $j_* = 1$. (b) Shear variance from each mode (circles) and the expected shear variance for each mode, based on (A12), the modal shapes in Fig. 6, and $j_* = 1$ (squares). In both panels the GM predictions were normalized to have the same total energy/shear variance as the data, summed over modes 1–5.

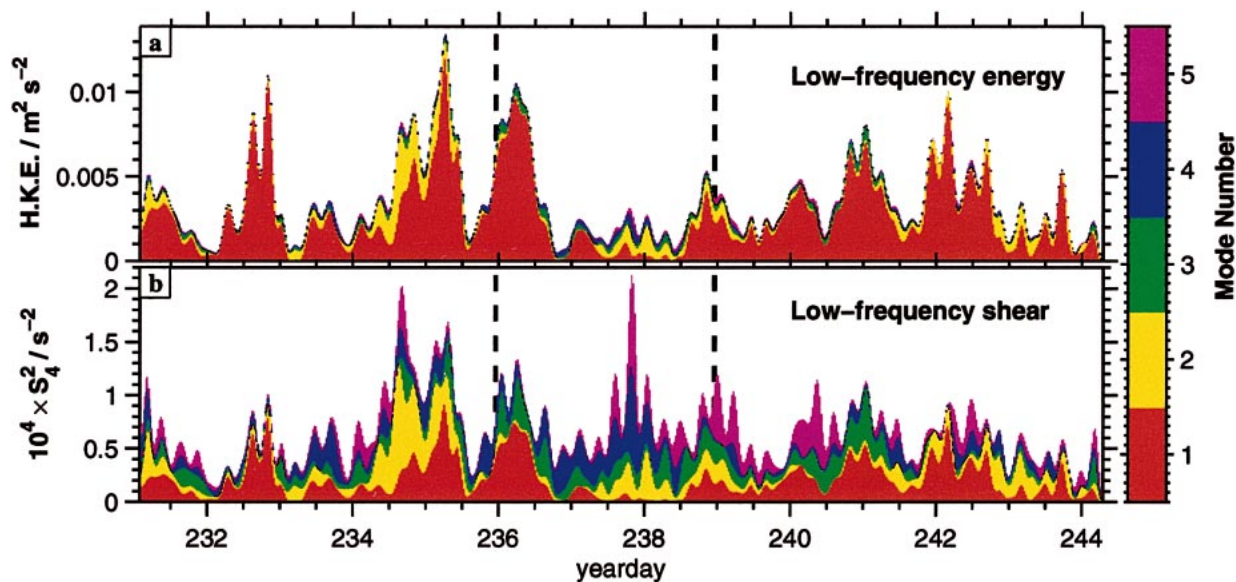


FIG. 9. Stacked histograms of (a) energy variance in first five baroclinic modes and (b) shear variance from the first five modes. The dotted lines indicate the times of the two sample profiles presented in Figs. 7 and 11.

plitude also affects the vertical distribution of shear relative to stratification, and consequently the Richardson number. For illustration, we return to the two profiles of Fig. 7. The energy and shear modal distributions for these times are shown in Figs. 11a,b. During the first time period (Fig. 11, left panels), shear was comparable to stratification in the thermocline (12–28 m), but dropped drastically below the thermocline (25–40 m). During the second time period (right panels), there was more energy and shear in high modes, specifically in mode 5. The result was a shear profile that was comparatively larger below the thermocline, occasionally rising high enough above stratification to potentially produce shear instabilities. The existence of a nonsteady spectrum also violates a crucial assumption behind wave–wave interaction based models of turbulence production. A revised dissipation rate parameterization that accounts for observed spectral properties is presented in MGa.

To be fair, spectral models like that of Garrett–Munk were never intended to represent low-frequency internal waves, especially the internal tide. Such models are successfully used in estimating turbulence in the open ocean because the majority of shear variance comes

from the continuum wavenumber range of the spectrum. However, on the continental shelf low-frequency waves are strong enough to independently produce order-1 Richardson numbers.

d. Solibores

One of the most interesting dynamical features observed on the summer shelf was the episodic passage of strongly nonlinear, high-frequency solibores. Energetic nonlinear internal solitary waves have been observed at a variety of locations around the world (Ostrovsky and Stepanyants 1989; Apel et al. 1995). In most cases, they are believed to be generated by interactions between tidal flow and steep topography. In a fluid with a strong pycnocline separating two comparatively well-mixed layers, theory and experiment predict a dominant mode-1 structure in baroclinic velocity, with an upper-layer flow in the direction of wave propagation (onshore for shelf waves), a bottom-layer flow in the opposite direction, and large (usually downward) isopycnal displacements centered in the thermocline (Apel et al. 1995).

We observed 15 solibores during our fortnight of ob-

TABLE 1. Correlation coefficients between model amplitudes squared (energy). The significance level based on the first zero-crossing of the autocorrelation sequence is ± 0.14 .

	Mode 0 (BT)	1	2	3	4	5
Mode 0 (BT)	1.00	−0.14	−0.16	−0.09	0.04	0.10
1	−0.14	1.00	0.14	0.12	−0.04	−0.08
2	−0.16	0.14	1.00	0.33	0.21	0.10
3	−0.09	0.12	0.33	1.00	−0.00	0.12
4	0.04	−0.04	0.21	−0.00	1.00	0.16
5	0.10	−0.08	0.10	0.12	0.16	1.00

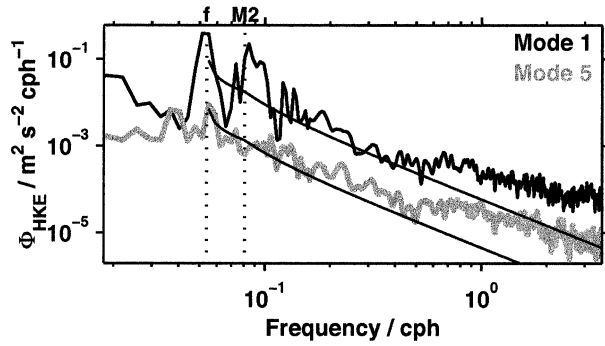


FIG. 10. Rotary spectra of kinetic energy in mode 1 (thin, black) and mode 5 (thick, gray) compared with idealized solutions from Levine (2002). Inertial and semidiurnal frequencies are indicated for reference.

servation, 5 of which occurred during microstructure profiling periods (Fig. 4). Though observed wave arrivals were consistent with a semidiurnal generation mechanism, there was huge variation in wave strength and properties from day to day. Solibores were picked out of the velocity record by hand based on a simple ad hoc criterion: events with depth-averaged baroclinic energies more than $2 \times 10^{-2} \text{ J kg}^{-1}$ above a 30-min running mean were classified as solibores. This criterion did not capture all bursts of high-frequency energy near wave crests, but did capture the major events. The duration of solibore events defined using this criteria ranged from 20 min to 4 h, with little apparent correlation between solibore duration and strength. The depth-averaged, event-averaged baroclinic horizontal kinetic energy ranged from 2.5×10^{-3} to $2.5 \times 10^{-2} \text{ J kg}^{-1}$. All 15 events consisted of strong shoreward flow in the upper water column and shelfward flow below, qualitatively consistent with two-layer soliton theory.

A particularly energetic event was observed on year-day 235. Northward velocity over a 24-h period including this time shows two packets of high-frequency energy (Fig. 12). Both packets were superimposed on the gradually varying internal tide. After the passage of each packet, local velocities, isopycnal displacements, and potential energy reflected a different phase of the internal tide (approximately one-quarter of a tidal period had elapsed), which provides some justification for the use of “solibore” rather than “soliton” (Henye and Hoering 1997). Velocity and shear contours of the larger, second packet are shown in the lower half of Fig. 12.

Profiles taken immediately before, and averaged during, the first three solibore troughs are shown in Fig. 13. Each pulse in the solibore packet brought strong on (off) shore velocities above (below) the thermocline and a large downward isopycnal displacement. The depth of the velocity zero-crossing (and maximum isopycnal displacements) during this and other observed solibores was 2–7 m lower than that of the linear first baroclinic mode, consistent with the fully nonlinear numerical simulations of Vlasenko et al. (2000). The large, quasi-

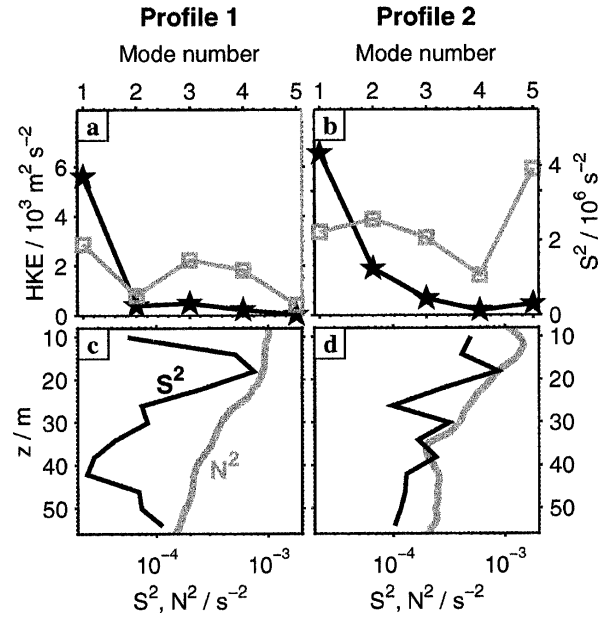


FIG. 11. (a), (b) Amplitude of energy (left axis, black stars) and shear variance (right axis, gray squares) in the first five baroclinic modes on yearday (left) 235.95 and (right) 238.96. (c), (d) Average vertical structures of shear variance (black) and buoyancy frequency (gray) during these periods (cf. Fig. 7).

two-layer flow in each wave trough produced a 2- to 10-fold increase in shear variance. Within wave troughs, the inverse Richardson number was pushed above the threshold for shear instability due to both large strains above the depth of peak displacement (15–25 m), and strong shear in the troughs (25–35 m; Fig. 13). Unlike the case of propagating internal waves, the depth ranges of peak shear and peak strain in these mode-1 standing waves are not collocated, resulting in two regions of supercritical Richardson number (Fig. 13e)

4. Energy flux

This section presents a description of energy fluxes through the CMO site from waves of different frequency and vertical mode. Energy flux is of interest for at least two reasons: it provides an upper bound on the energy available for dissipation and turbulent mixing upshelf, and it can be compared with local rates of energy dissipation to estimate characteristic propagation distances for specific waves and hence shed light on the dynamics of the local internal wave field. Below we discuss several methods of calculating energy flux and present resultant fluxes for distinct vertical modes, low-frequency waves, and solibores.

a. Methods

The change in energy at a given location (neglecting turbulent decay) can be written as the divergence of an energy flux,

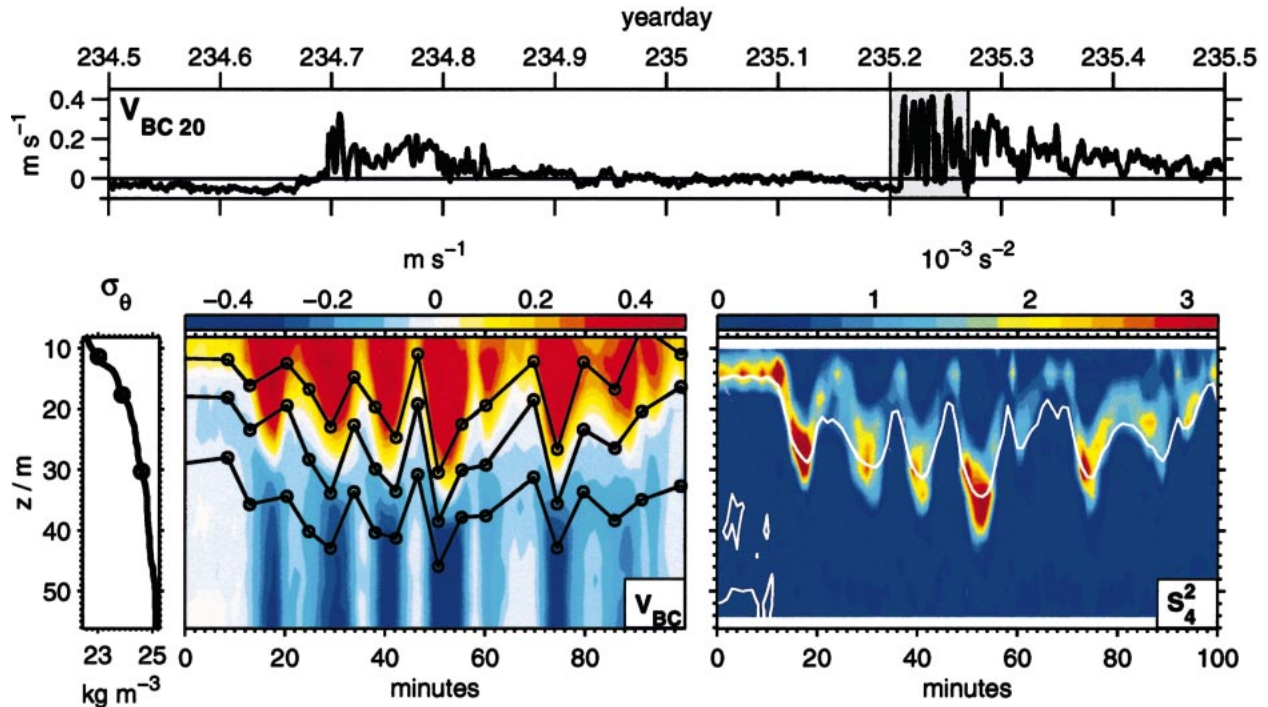


FIG. 12. (top) Baroclinic northward velocity at 20-m depth over 1 day. (bottom left) The presolibore density profile from yearday 235.19. (bottom middle) Contoured baroclinic northward velocity in depth and time for a subset of time corresponding to the shaded area in the top panel. Time is measured in minutes from yearday 235.2. The displacements of three isopycnals are superimposed, with circles indicating MMP measurement times. (bottom right) Four-meter shear variance during this same period, overlain by the zero isotach contour (white).

$$\frac{\partial E}{\partial t} = -\nabla \cdot \mathbf{F}. \quad (4)$$

For a propagating internal wave, energy-flux can be written two different ways, dubbed \mathbf{F}_1 and \mathbf{F}_2 ,

$$\mathbf{F}_1 = \overline{E\mathbf{c}_g} + \overline{E\mathbf{u}'} \quad (5)$$

$$\mathbf{F}_2 = \overline{p'\mathbf{u}'} + \overline{E\mathbf{u}'}, \quad (6)$$

where E represents total (kinetic plus potential) baroclinic energy density, \mathbf{c}_g is the group velocity, and \mathbf{u}' , p' are perturbation wave velocity and reduced pressure. All quantities are averaged over the water-column depth and should be averaged in time over a wave period (Kunze et al. 2002). The second term in each equation represents the advection of wave energy by wave velocity, and is neglected in the limit of linear waves. Both

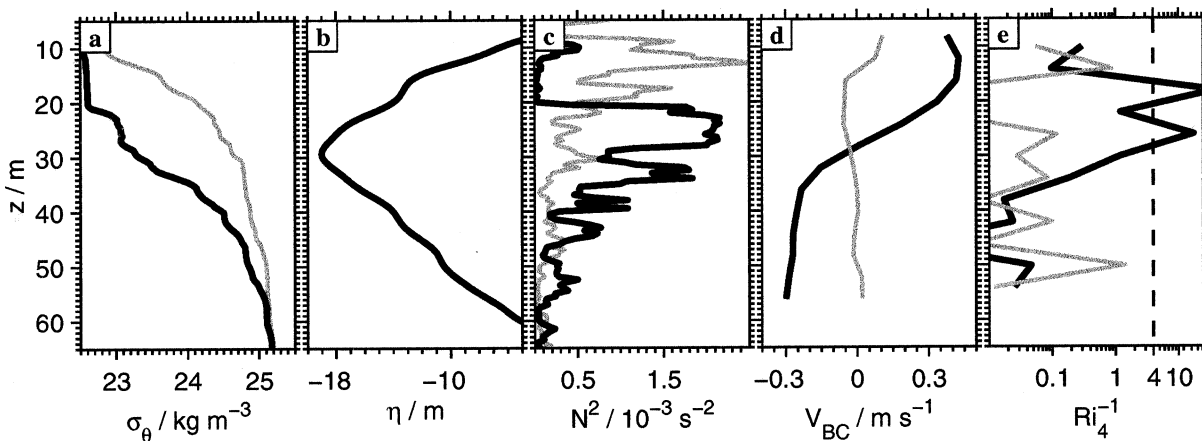


FIG. 13. Profiles of various quantities immediately before (thin, gray) and during the first three troughs of the yearday-235 solibore (thick, black): (a) potential density, (b) isopycnal displacement between the two density profiles shown in (a), (c) buoyancy frequency, (d) northward baroclinic velocity, and (e) Richardson number based on 4-m shear and stratification.

TABLE 2. Energy flux (W m^{-1}) calculated using (5), \mathbf{F}_1 , and (6), \mathbf{F}_2 . In each case flux is divided into contributions from the first five vertical modes (across) and from different frequency bands (down): all frequencies, semidiurnal (SD), near-inertial (NI), and solibores. For the second method, total flux direction is also calculated.

	Total	Mode 1	2	3	4	5
(a) \mathbf{F}_1 total	129.7	106.8	14.7	4.3	2.4	1.5
(b) F_1 NI	3.4	2.0	0.7	0.3	0.3	0.0
(c) F_1 SD	64.7	57.8	5.7	0.7	0.3	0.16
(d) F_1 solibore	12.1					
(e) \mathbf{F}_2 total	137.2	116.5	13.4	5.0	1.5	0.9
(f) F_2 angle ($^\circ$ from W)	79.9	77.1	107.3	100.3	70.7	-25.0
(g) F_2 solibore	4.0					

methods are used here to compute energy fluxes and will subsequently be referred to as method one and method two. For the first method, \mathbf{F}_1 , energy density and group velocity are calculated based on ADCP-measured velocity variance and vertical mode shape, using the dispersion relation. For the second method, \mathbf{F}_2 , perturbation (baroclinic) velocity estimates from the ADCP are combined with perturbation pressure estimates from the microstructure profiler. With either method, the difficult task remains of deciding what period to average over in a wave field where near-inertial, semidiurnal, and high-frequency waves all contribute substantial energy (Fig. 5). The first method capitalizes on the excellent temporal resolution of the ADCP to bandpass velocity, and hence to separate flux from different frequency waves. However, when simply looking at energy densities, flux direction cannot be determined and, in fact, propagating waves cannot be distinguished from horizontal standing waves, which have no associated energy flux. Thus, calculations using this method represent an upper bound. On the other hand, the second method robustly determines energy-flux magnitude and direction, but is limited by the noncontinuous (12 hours on, 12 hours off) nature of MMP sampling.

b. Flux results

For the first method, \mathbf{F}_1 , energy density of each mode is multiplied by the appropriate group speed for that mode. For a given mode, the total energy (horizontal and vertical kinetic energy plus potential energy) is related to the measured horizontal kinetic energy by a frequency-dependent correction function,

$$\frac{E_j(\omega)}{\text{HKE}_j(\omega)} = \left[1 + \frac{\text{VKE}_j(\omega) + \text{PE}_j(\omega)}{\text{HKE}_j(\omega)} \right] \quad (7)$$

$$= \left[1 + \frac{\omega^2 - f^2}{\omega^2 + f^2} \left(1 + \frac{\omega^2}{c_j^2} \frac{\int \Psi_j^2}{\int \Psi_j'^2} \right) \right], \quad (8)$$

where Ψ_j , c_j are defined in (2). Group speed, $c_g = \partial\omega/\partial k$, is a function of frequency and mode number (Gill

1982). Energy flux is calculated for each vertical mode as a function of frequency by multiplying the rotary frequency spectra of each modal amplitude and group velocity and integrating over the internal wave band. The total energy flux for each mode is given in Table 2a. Fluxes from near-inertial (1–1.6 cpd) and semidiurnal (1.7–2.5 cpd) bandpassed waves are shown in Tables 2b,c. The overwhelming majority of flux was due to first-mode waves; the dramatic decrease in energy flux with increasing mode number reflected both the declining energy (Fig. 8) and decreasing group speed of higher modes. Half the total flux was from the semidiurnal band. Though there was comparable energy in near-inertial and semidiurnal waves (Fig. 5), the lower group velocity of near-inertial waves resulted in a order of magnitude lower energy flux.

During MMP profiling periods we computed an alternate estimate of energy flux, \mathbf{F}_2 , using perturbation pressure measurements from the microstructure profiler (Fig. 3). Velocity and pressure perturbation were both projected onto vertical modes to calculate a mode-by-mode estimate of energy flux (Table 2e). This method allowed resolution of eastward and northward components of energy flux separately, giving flux direction as well as magnitude (Table 2). The majority of energy flux was propagating onshore, roughly perpendicular to isobaths. On the whole, the two methods of calculating energy flux agree remarkably well, suggesting that the overwhelming majority of observed energy was from propagating (as opposed to horizontally standing) internal waves.

c. Solibore energy fluxes

Both methods of calculating energy flux allow estimates of energy flux during solibores, although using the second method we only have observations of 5 of 15 total events. For both methods, solibore energy fluxes were calculated using high-passed (above 4 cpd) velocity averaged over each solibore period (section 3d) and depth-integrated. The nonlinear terms from (5) and (6) were also included for these large-amplitude waves. The calculation of perturbation pressure (1) assumes the hydrostatic approximation, which may not be appropriate for high-frequency solibores; energy fluxes cal-

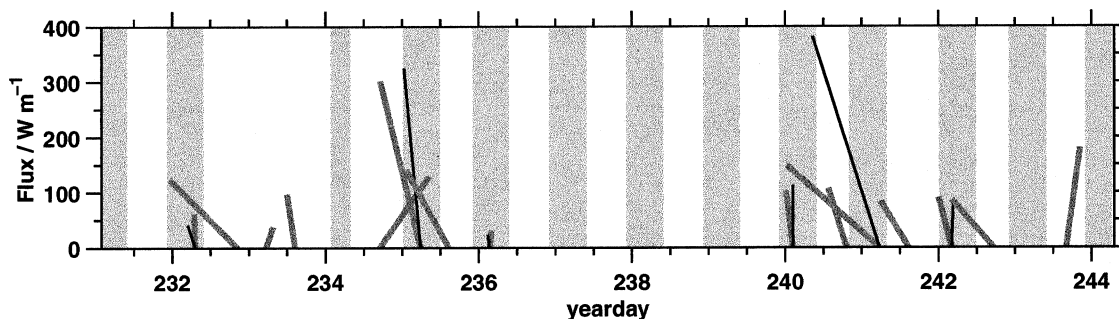


FIG. 14. Average energy flux during solibores; each line is based on the midpoint time of that event and shows the magnitude (units given on the vertical axis) and direction of flux. Fluxes based on (5) (thick, gray) are assumed to be in the direction of strongest velocity. Fluxes based on (6) (thin, black) are calculated only during MMP profiling periods indicated by gray shading.

culated here may be underestimates. It is assumed that solibores propagate at the group speed of high-frequency first-mode waves, 0.45 m s^{-1} , plus a correction term for their nonlinear amplitude (Apel et al. 1995). For the range of solibores observed (10–20-m peak vertical displacements), nonlinearity increased the estimated group speed to $0.48\text{--}0.52 \text{ m s}^{-1}$. Comparison of shipboard, mooring and satellite data results in group speed estimates of $0.4\text{--}0.6 \text{ m s}^{-1}$ (Zheng et al. 1993; Pringle and Brink 1999; Colosi et al. 2001).

Though only present for 10% of the time, cruise-averaged solibore fluxes were a fifth of the strength of the semidiurnal internal tide flux (Table 2d). Energy fluxes averaged over the duration of particular solibore events were larger and highly variable in magnitude (Fig. 14); there was a reasonable agreement in flux magnitude calculated using the two methods for most solibore events. The lower cruise-averaged energy flux using the second method (Table 2g) reflects the random subsample of events observed during profiling periods—the largest events are included but not the majority of midsize events (Fig. 14: yeardays 233, 234.5, 235.5, and 243.5). There was a range of around 40° of flux direction. Synthetic aperture radar (SAR) images taken during and before the experiment reveal surface signatures of solibore packets propagating shoreward in different directions, suggestive of several different generation sites along the shelfbreak (D. Thompson 2001, personal communication).

d. Implications of energy fluxes

Observations of energy fluxes give an upper bound on baroclinic energy available to dissipate farther up-shelf. For example, if the total observed energy flux of 130 W m^{-1} were evenly dissipated over 100 km (roughly the distance to the coast) in an ocean that was on average 40 m deep, the average dissipation rate would be $3 \times 10^{-8} \text{ W kg}^{-1}$, comparable to that observed at the CMO site (MGa). For comparison, Holloway et al. (2001) studied the propagation of the M_2 internal tide onto the North West Australian shelf and observed on-shore energy fluxes that decayed with distance, ranging

from 1 W m^{-1} at the 300-m isobath to 0.5 W m^{-1} at 124 m to negligible flux at 65 m.

Alternately, a rough estimate of characteristic distances traveled by different types of waves can be calculated by dividing energy flux by a typical rate of turbulent energy dissipation. MGa observe an average dissipation rate of $10^{-8} \text{ W kg}^{-1}$ away from the surface and bottom frictional boundary layers. In a steadily dissipating shelf of constant (70 m) depth, the first-mode internal tide could propagate 90 km, while near-inertial waves and mode-5 waves could propagate only 4.7 and 2.1 km, respectively (Table 2). This result has important implications for modeling internal-wave energy and shear on a shelf; while the internal tide is a shelfwide phenomenon, shear-containing near-inertial waves and higher-mode waves, both of which may be important for turbulence generation (MGa), were probably generated locally. However, this simple calculation ignores huge variations in turbulence strength, which was in turn systematically linked to internal wave strength (MGa). Furthermore, dissipation may not be draining energy equally from all modes. If anything, turbulence is expected to drain energy most efficiently from higher modes (Polzin et al. 1995).

Dissipation may also be an important component of solibore energetics. Solibores experiencing the average dissipation rate could propagate hundreds of kilometers without being significantly drained of energy (Table 2). However, the appropriate dissipation rate to use for these waves varies between solibore events and, in general, is significantly higher than the average dissipation rate used here (MGa). The dissipation rate in the strongest solibores was large enough to significantly erode their energy over one day, which was also the length of time the waves observed to propagate onshore before disappearing near the 40-m isobath (MGa; D. Thompson and J. Barth 2001, personal communication). On the other hand, Henyey and Hoering (1997) argue that, in a borelike wave, steady dissipation can be balanced by a constant energy supply to the wave from net changes in isopycnal locations and potential energy, which in our case could be from the larger-scale internal tide.

5. Conclusions

This study has described the local characteristics and flux of baroclinic energy and shear from internal waves on a shelf. The goal of this paper and the companion paper is to compare and contrast the relationship between internal waves and turbulence on a continental shelf and that in a steady-state open ocean environment. Here we have shown that the internal wavefield on the New England shelf diverges in several significant ways from the wave properties assumed in steady-state spectral models. The most noticeable difference is the presence of energetic, high-frequency solibores (section 3d). High shear and strain with each trough of these mode-1 waves lowered the Richardson number below the threshold for shear instability. Even apart from the solibores, observed internal waves could not be characterized by a well-defined, slowly evolving spectral shape. Instead, we found the following:

- The energy content of different frequency and vertical mode waves evolved substantially and independently during the cruise. The amplitudes of distinct vertical modes differed in frequency content, implying a non-separable spectrum (Fig. 10). Even among low-frequency waves, the relative and absolute magnitudes of different modes varied by an order of magnitude on timescales of days to weeks (Fig. 9). The implication is that the time varying energy in low- and high-mode waves are not correlated (Table 1), violating a major assumption behind many internal-wave-based turbulence parameterizations (MGa).
- Shear variance from this low-frequency, low-mode wave field was on average concentrated in the thermocline. However, both the absolute magnitude and stratification normalized strength of shear varied as the energy in each mode evolved. As a result of large changes in the relative amplitudes of each mode, the depth-integrated magnitude of shear variance and depth-dependent Richardson number were decoupled from the low-mode dominated energy density (Fig. 9). For example, during periods when high-mode waves were present, shear was relatively large (as compared with energy) and was spread out over a range of depths below the thermocline (Figs. 2, 9, 11).

There are two main conclusions of the energy-flux calculations presented here. First, the energy flux was primarily due to the internal tide, in both linear and nonlinear (solibore) forms, and propagated generally onshore through a wide range of angles. If the energy density observed to be propagating onshore is posited to be steadily lost before reaching the coast, the resultant average dissipation rate would be comparable to that

observed locally by MGa. Second, comparison of the average measured dissipation rate and energy fluxes from different waves suggests that both near-inertial waves and higher-mode waves were generated locally.

Acknowledgments. We thank Jody Klymak, Earl Krause, Jack Miller, Gordon Welsh, and the entire crew of the R/V *Seward Johnson* for help with data collection. Numerous other CMO investigators generously shared their thoughts and results with us. We particularly thank Wilf Gardner, Murray Levine, Tim Boyd, Jack Barth, Steve Anderson, James Edson, Al Plueddemann, Steve Lentz, Steven Babin, and Ray Sterner. The thoughtful comments of an anonymous reviewer were helpful in focusing the results and implications of this work. This work was supported by ONR Grant N00014-95-1-0406. Jennifer MacKinnon received additional support from an NDSEG research fellowship. Michael Gregg received additional support from the SECNAV/CNO Chair in Oceanography.

APPENDIX

Vertical Modes

Velocity may be decomposed onto orthogonal vertical modes, $\Psi'(z)$, that are eigensolutions to the Taylor–Goldstien equation with no mean vertical shear (2). The modes satisfy depth-integrated normalization conditions,

$$\int_{-H}^0 \Psi_j(z)\Psi_k(z) \left[\frac{N^2(z)}{\omega^2 - f^2} \right] dz = D(\psi)\delta_{jk} \quad (A1)$$

$$\int_{-H}^0 \Psi'_j(z)\Psi'_k(z) dz = D(\omega)\delta_{jk}, \quad (A2)$$

where D is the Wentzel–Kramers–Brillouin (WKB) stretched waveguide thickness, which for waves with frequencies everywhere greater than the buoyancy frequency is simply the WKB stretched water depth (Levine 2002).

In a statistically stationary wave field, Levine (2002) suggests that hydrostatic wave energy can be represented by a modified version of the Garrett–Munk spectrum that accounts for the importance of vertical boundaries and turning points in coastal regions, resolves inconsistencies with latitudinal scaling, and clarifies the physical meaning of scaling constants for comparison between coastal and open ocean regimes. In Levine’s model, total energy (kinetic and potential) at a given depth is given by

$$\text{HKE}(z) + \text{PE}(z) = \int_f^{N_0} \sum_j \left[\frac{1}{2} \left(\frac{\omega^2 + f^2}{\omega^2} \right) \frac{\Psi'_j(z)^2}{\alpha_j^2} + \frac{1}{2} \frac{N^2}{\omega^2} \Psi_j^2(z) \right] [E_{\text{ref}} H(j) \hat{B}(\omega)] d\omega, \quad (A3)$$

where E_{ref} represents the total energy divided by the vertical waveguide thickness and is roughly equivalent to $E_{\text{gm}} b^2 N_0^2$ in the traditional GM spectrum. Here H_j represents the relative distribution of energy among vertical modes (Munk 1981),

$$H_j = \frac{1}{J} \left(\frac{1}{j_*^2 + j^2} \right) \quad (\text{A4})$$

with

$$J = \sum_j \frac{1}{j_*^2 + j^2}. \quad (\text{A5})$$

Levine argues that $j_* = 1$ is more appropriate for the coastal ocean than the traditional value of $j_* = 3$; $\hat{B}(\omega)$ is a revised version of the GM $B(\omega)$ that preserves spectral amplitude across different latitudes.

In a nonstationary wave field, it is often more useful to consider a time-varying wave energy rather than integrating a steady frequency spectrum. Focusing on kinetic energy alone,

$$\begin{aligned} \text{HKE}(z, t) &= \sum_j A_j(t) \Psi_j'^2(z) \frac{H}{D} \\ &+ \sum_{j \neq k} \sum X_{jk}(t) \Psi_j'(z) \Psi_k'(z) \frac{H}{D}, \quad (\text{A6}) \end{aligned}$$

where $A_j(t)$ is the energy in each mode, X_{jk} represents the interference between modes, and H is the water depth (not to be confused with H_j). Depth averaging allows us to apply the orthogonality condition (A1) to eliminate the cross term,

$$\overline{\text{HKE}(t)} = \frac{1}{H} \int_{-H}^0 \text{HKE}(z, t) dz = \sum_j A_j(t) \quad (\text{A7})$$

$$= E(t) \sum_j H_j(t), \quad (\text{A8})$$

where for comparison with other models we have divided the sum of modal energy into a total energy level, $E(t)$, and a relative contribution from each mode, $H_j(t)$.

Shear variance at each depth is given by

$$\begin{aligned} S^2(z, t) &= \sum_j A_j(t) \Psi_j''(z)^2 \frac{H}{D} \\ &+ \sum_{j \neq k} \sum X_{jk}(t) \Psi_j''(z) \Psi_k''(z) \frac{H}{D}. \quad (\text{A9}) \end{aligned}$$

Depth-averaging and assuming the cross-term is small (for our data the interference of shear from different modes on average contributed less than 4% to total shear variance),

$$\begin{aligned} \overline{S^2(t)} &= \sum_j A_j(t) \frac{1}{D} \int_{-H}^0 \Psi_j''(z)^2 dz \\ &+ \sum_{j \neq k} \sum X_{jk}(t) \int_{-H}^0 \Psi_j''(z) \Psi_k''(z) \frac{1}{D} dz \quad (\text{A10}) \end{aligned}$$

$$\approx \sum_j A_j(t) \frac{1}{D} \int_{-H}^0 \Psi_j''(z)^2 dz \quad (\text{A11})$$

$$= E(t) \sum_j H_j(t) \frac{1}{D} \int_{-H}^0 \Psi_j''(z)^2 dz. \quad (\text{A12})$$

For a simple case of linear stratification, the $\Psi(z)$ are pure sinusoids, and the relationship between the depth-averaged energy and shear variance of each mode is given by

$$\frac{1}{H} \int_{-H}^0 \Psi_j''(z)^2 \frac{H}{D} dz = \frac{\pi^2}{H^2} j^2. \quad (\text{A13})$$

REFERENCES

- Alford, M., and R. Pinkel, 2000: Observations of overturning in the thermocline: The context of ocean mixing. *J. Phys. Oceanogr.*, **30**, 805–832.
- Apel, J., L. Ostrovsky, and Y. A. Stepanyants, 1995: Internal solitons in the ocean. Applied Physics Laboratory Tech. Rep. ME-RJRA0695, The Johns Hopkins University, 70 pp.
- Chapman, D. C., and R. C. Beardsley, 1989: On the origin of shelf water in the Middle Atlantic Bight. *J. Phys. Oceanogr.*, **19**, 384–391.
- Colosi, J., R. C. Beardsley, J. Lynch, G. Gawarkiewicz, C.-S. Chiu, and A. Scotti, 2001: Observations of nonlinear internal waves on the outer New England continental shelf during the summer shelfbreak PRIMER study. *J. Geophys. Res.*, **106**, 9587–9602.
- Gardner, W., and Coauthors, 2001: Optics, particles, stratification, and storms on the New England continental shelf. *J. Geophys. Res.*, **106**, 9473–9497.
- Gill, A. E., 1982: *Atmosphere–Ocean Dynamics*. Academic Press, 662 pp.
- Gregg, M. C., 1989: Scaling turbulent dissipation in the thermocline. *J. Geophys. Res.*, **94**, 9686–9698.
- Henyey, F. S., and A. Hoering, 1997: Energetics of borelike internal waves. *J. Geophys. Res.*, **102**, 3323–3330.
- Holloway, P. E., P. G. Chatwin, and P. Craig, 2001: Internal tide observations from the Australian North West shelf in summer 1995. *J. Phys. Oceanogr.*, **31**, 1182–1199.
- Kunze, E., L. K. Rosenfeld, G. S. Carter, and M. C. Gregg, 2002: Internal waves in Monterey Submarine Canyon. *J. Phys. Oceanogr.*, **32**, 1890–1913.
- Levine, M. D., 2002: A modification of the Garrett–Munk internal wave spectrum. *J. Phys. Oceanogr.*, **32**, 3166–3181.
- MacKinnon, J., and M. Gregg, 2003a: Mixing on the late-summer New England shelf—Solibores, shear, and stratification. *J. Phys. Oceanogr.*, **33**, 1476–1492.
- Miles, J., 1961: On the stability of heterogenous shear flows. *J. Fluid Mech.*, **10**, 496–512.
- Munk, W. H., 1981: Internal waves and small-scale processes. *Evolution of Physical Oceanography*, B. A. Warren and C. Wunsch, Eds., The MIT Press, 264–291.
- Ostrovsky, L., and Y. A. Stepanyants, 1989: Do internal solitons exist in the ocean? *Rev. Geophys.*, **27**, 293–309.
- Polzin, K. L., J. M. Toole, and R. W. Schmitt, 1995: Finescale parameterizations of turbulent dissipation. *J. Phys. Oceanogr.*, **25**, 306–328.
- Pringle, J. M., and K. H. Brink, 1999: High-frequency internal waves on a sloping shelf. *J. Geophys. Res.*, **104**, 5283–5299.
- Sandstrom, H., and N. Oakey, 1995: Dissipation in internal tides and solitary waves. *J. Phys. Oceanogr.*, **25**, 604–614.
- Sundermeyer, M., and J. Ledwell, 2001: Lateral dispersion over the continental shelf: Analysis of dye-release experiments. *J. Geophys. Res.*, **105**, 9603–9621.
- Thorpe, S., 1998: Estimating internal waves and diapycnal mixing

- from conventional mooring data in a lake. *Limnol. Oceanogr.*, **43**, 936–945.
- Thorpe, S. A., 1978: On the shape and breaking of finite amplitude internal gravity waves in a shear flow. *J. Fluid Mech.*, **85**, 7–32.
- Vlasenko, V., P. Brandt, and A. Rubino, 2000: Structure of large-amplitude internal solitary waves. *J. Phys. Oceanogr.*, **30**, 2172–2185.
- Voorhis, A., D. Webb, and R. Millard, 1976: Current structure and mixing in the shelf/slope water front south of New England. *J. Geophys. Res.*, **81**, 3695–3707.
- Zheng, Q., X.-H. Yan, and V. Klemas, 1993: Statistical and dynamical analysis of internal waves on the continental shelf on the Middle Atlantic Bight from space shuttle photographs. *J. Geophys. Res.*, **98**, 8495–8504.